# On the Assessment and Rationalization of Heterogeneous Nucleation in Investment Cast Superalloys

RICHA GUPTA, BEN GOODYER, DMYTRO SHEVCHENKO, ROGER REED, JOSEPH MOSES, NILS WARNKEN, OWEN DRAPER, and NICK GREEN

Liquid metal/ceramic reactions are studied using an experimental arrangement reliant on differential scanning calorimetry. The undercooling needed to stimulate solidification is shown to depend strongly not only upon the chemistry of the ceramic but also the oxygen partial pressure. Ceramics based upon $Y_2O_3$ and related compounds are emphasized. Characterization using electron microscopy of the interfacial reaction products is used to rationalize the reaction pathways. Our results shed light on the importance of the ceramic mould chemistry in promoting nucleation in these systems. This insight carries significant implications for practical applications, including (i) evaluating zircon sources and impurity effects; (ii) developing new mould formulation less prone to secondary grain nucleation in casting regions isolated from the advancing solidification front; and (iii) identification of grain refiners tailored for equiaxed solidification in superalloy castings.

https://doi.org/10.1007/s11661-025-08057-z


## I. INTRODUCTION

NUCLEATION is the process by which one phase forms from another. It is a stochastic process, implying randomized fluctuations on the scale of the microstructure with associated evolution and decay of nuclei until a critical size is attained.[1–4] There is usually debate about whether homogeneous nucleation can indeed arise and thus whether heterogeneous nucleation is more applicable in practice; this is because the rate of nucleation is usually very sensitive to the structure and chemistry of surfaces, which represent nucleation sites often potent enough to reduce the activation energy needed and thus the size of the critical nucleus.[5–10] Traditionally, classical nucleation theory has been invoked as the standard against which any new theories are judged; recently other non-classical treatments have been proposed which are successful in explaining some of its shortcomings.[11–18]

In this paper, we study the nickel-based superalloys which are often grown in monocrystalline form from the liquid state. Here, nucleation is important because if it occurs once steady-state growth has been established then properties are compromised; this is because it leads inevitably to stray grains and thus grain boundaries which are deleterious to creep or fatigue.[19–23] This situation is unusual in the sense that one wants to anticipate the nucleation event so that one can design against it—in this instance it is unfavourable, in contrast to the grain refining effect for which nucleation is stimulated. Here, the nucleation process is particularly sensitive to the ceramic mould material employed during investment casting.[24–26] When nucleation does indeed occur—for example from undercooled regions ahead of the moving growth front or else from ceramic particles which become detached from the mould during filling—the so-called casting defects are deemed fatal since they cannot be tolerated. But despite the importance of this phenomenon, there is very little systematic experimentation on this topic so far.[4,7] Here, an experimental approach is used which makes use of precise control using differential scanning calorimetry.

Sessile drop tests have been widely used to study the liquid metal–solid substrate interaction and wetting behaviour, particularly to assess the nucleation potency of the substrate. Kanetkar *et al.*[24] first investigated various Ni alloys on $Al_2O_3$, $HfO_2$, and $Y_2O_3$ substrates,

RICHA GUPTA, BEN GOODYER, DMYTRO SHEVCHENKO, JOSEPH MOSES, NILS WARNKEN, and NICK GREEN are with the University of Birmingham, Birmingham B152TT, UK. Contact e-mail: Nick.Green@htrc.bham.ac.uk ROGER REED is with the University of Birmingham and also with the University of Oxford, Oxford OX12JD, UK. OWEN DRAPER is with the Rolls-Royce Plc, Derby DE217BE, UK.
Manuscript submitted September 19, 2025; accepted November 20, 2025.



Published online: 12 January 2026

and found non-wetting to marginal wetting behaviour of alloys on $HfO_2$ and $Y_2O_3$. Later studies by Zi *et al*.,[27] Li *et al*[10] focussed on Ni-based superalloys with varying Re content and trace impurities content, and their interaction with $Al_2O_3$-based ceramic substrate. Recent work by Akmal *et al*.[7] compared the metal–mould interaction between Hf containing and Hf-free superalloys with $Al_2O_3$-based ceramic mould, using a directional solidification full-scale casting experiment. While informative, these methods are experimentally intensive, costly, and often lack the thermal precision needed to isolate nucleation events. In contrast, this study introduces a differential scanning calorimetry (DSC)-based approach that enables precise thermal control and high sensitivity to exothermic nucleation signals, allowing for the systematic probing of the onset of nucleation under controlled undercooling conditions. This method offers a more accessible platform for evaluating nucleation potency across different ceramic mould chemistries.

## II. EXPERIMENTAL DETAILS

The research here has made extensive use of differential scanning calorimetry (DSC), with emphasis on solidification of CMSX-4 on pure yttria ($Y_2O_3$), and yttria-doped in standard face coat slurry mainly consisting of zircon flour ($ZrSiO_4$)/colloidal silica ($SiO_2$) [with an additional antifoaming and wetting agent in desired proportions]. A standard $ZrSiO_4/SiO_2$ face coat slurry was also used for benchmarking purpose. High purity alumina crucibles of volume 85 $\mu$l were used for all measurements and coated to thicknesses of 20-40 $\mu$m. The three steps involved (i) crucibles being filled with the $ZrSiO_4/SiO_2$ face coat slurry by using a pipette and the excess slurry drained out; or (ii) high-purity $Y_2O_3$ being applied in the form of an aerosol-based sol to the crucibles; or (iii) 4.5 wt pct of $Y_2O_3$ particles of size $D_v(50) - 26.2$ $\mu$m being mixed into $ZrSiO_4/SiO_2$ face coat slurry prior to application. The coated crucibles were dried at room temperature for 24 hours followed by firing in air at 873 K for 1 hour. Cylindrical samples of the as-cast CMSX-4 of diameter 4 mm and thickness 1 mm (mass 70-90 mg) were placed inside the prepared crucibles. These were polished and cleaned with isopropanol before performing the DSC test.

Differential scanning calorimetry (DSC) was performed on a Netzsch STA 449 F3 Jupiter, equipped with automatic sample changer and high-temperature furnace with capability to 1923 K. A two-stage heating and cooling protocol was developed, involving heating from 1173 K at 10 K/min to 1763 K (follow temperature equilibration) followed by cooling at 10 K/min to 1173 K. The first heating cycle was used to facilitate wetting of the crucible by the CMSX-4 sample and to break down the as-cast structure. This was characterized by a total liquid contact time of 4980 seconds, defined as the period during which the sample exceeded the solidus temperature. To study the kinetics of transformation/reaction pathways, the liquid contact time with pure $Y_2O_3$ coating was reduced systematically. Here, DSC measurements were also carried out using (i) a two-stage thermal cycle involving heating from 1173 K to 1763 K, holding for 10 minutes, followed by cooling back to 1173 K at 25 K/min, this results in a total liquid contact time of 2280 seconds. Furthermore, (ii) a single heating and cooling cycle also spans the temperature range of 1173 K to 1763 K, holding for 5 minutes, and cooling to 1173 K, with cooling rates set at 25 K/min, yielding a liquid contact time of 1140 seconds.

To investigate the significance of oxygen, DSC measurements were carried out in two furnace conditions: in flowing Ar atmosphere (Ar with grade 6 purity), and with addition of a zirconium oxygen trap system (OTS) supplied by Netzsch to further reduce the oxygen levels in the furnace. As a further substantiation of the developed DSC approach for metal–mould interaction, pure $Y_2O_3$-coated DSC crucibles with CMSX-4 were melted in a production Bridgman single-crystal casting furnace using the standard casting parameters, furnace hot zone temperature 1793 $\pm$ 15 K, a holding time of 4500 s, and vacuum of $10^{-4}$ mbar. The samples were fast withdrawn to room temperature after holding. The distance between ceramic plate and the copper chill was 200 mm, therefore the chill plate has no effect on sample temperature. Prior to solidification, the coated DSC crucibles were mounted on a ceramic plate as discussed in Section IV–A. CMSX-4 samples were placed inside and the crucibles covered with lids. The entire arrangement was processed in the furnace and metal/coating interface subsequently analysed.

The nucleation undercooling ($\Delta T_n$) was estimated from the DSC curves in the following way. Two major peaks were displayed, one corresponding to melting during the heating cycle and the other to solidification during cooling cycle—see Figure 1. The nucleation undercooling in the present work was defined as the difference in the endothermic peak during heating ($T_m$) and onset of solidification ($T_s$), as determined from the first derivative (DDSC) of the cooling curve. For each material combination, a minimum of five experiments were undertaken—and in some cases more than this—in order to assure repeatability and establish scatter in the values measured.

Since a major aim of this work has involved the study of the reaction layer formed of the metal/ceramic interface, the DSC samples were mounted perpendicular to the crucible contact surface (see Figure 2) in conductive bakelite, subsequently ground and polished before final polishing with colloidal silica suspension of 0.25 $\mu$m. The interfacial reaction products were examined by using Jeol 7000F field emission gun-scanning electron microscope (FEG-SEM) equipped with energy dispersive spectroscopy (EDS). To promote the elemental contrast, imaging was carried out in backscatter electron (BSE) mode at 20 kV operating voltage. For chemical composition analysis, EDS elemental mapping was performed.

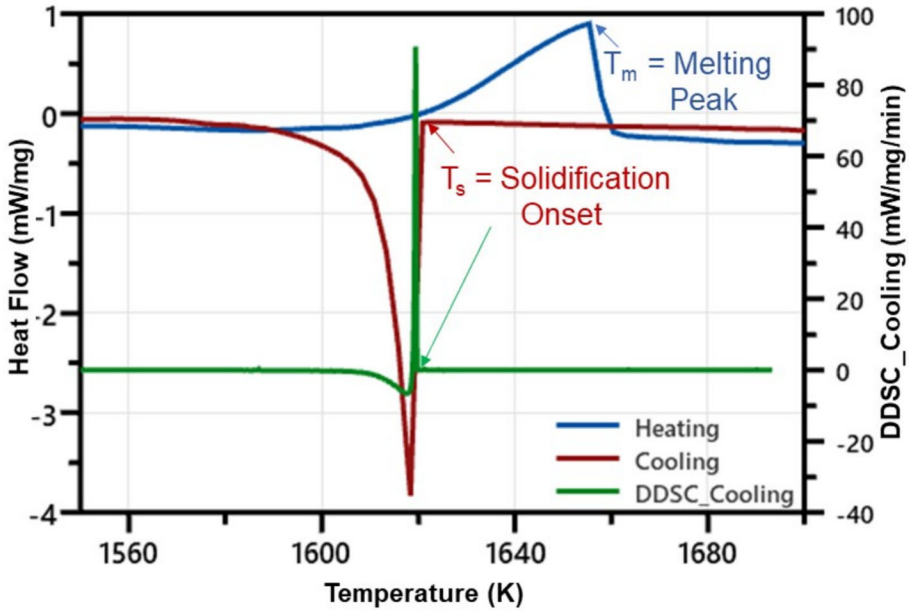


Fig. 1—DSC curve obtained during the heating and cooling cycle. The terms $T_m$ and $T_s$ represent the temperatures corresponding to the melting peak and start of solidification, respectively, and DDSC is the first derivation of the DSC signals on cooling.

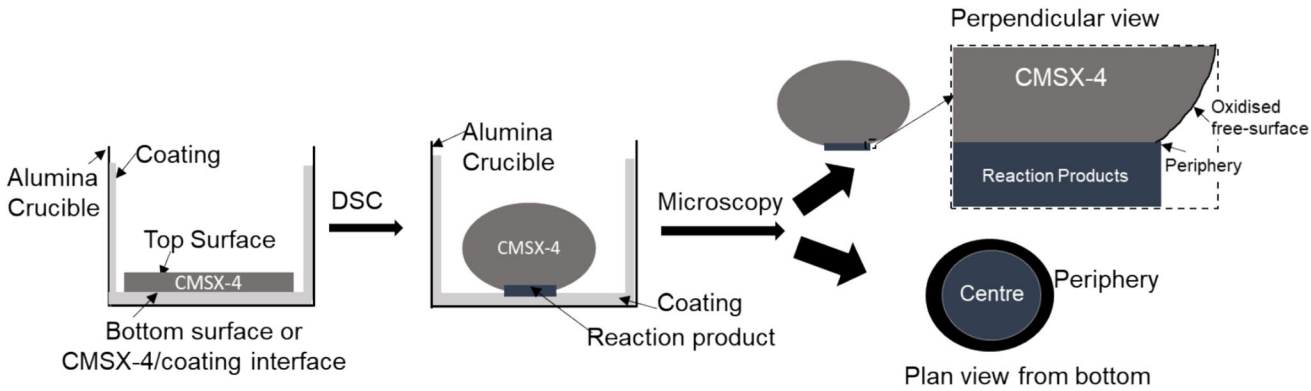


Fig. 2—Schematic diagram showing the description of experimental approach for microscopy characterization of the reaction layer.

## III. RESULTS

### A. *Nucleation Undercooling*

The calorimetry has revealed some fascinating effects of oxygen partial pressure on nucleation behaviour. In general, the heating curves confirmed that the liquidus temperature (melting peak) ($T_m$) was largely unaffected by the presence/absence of the oxygen trap system (OTS) in the furnace. However, the solidification temperature ($T_s$) was found to vary significantly depending on furnace oxygen levels, resulting in a corresponding variation in nucleation undercooling, $\Delta T_n = T_m - T_s$, as shown in Figures 3 and 4(a). The data obtained from DSC are summarized in Tables I and II, for five tested samples in each case.

The application of the OTS was found to increase $\Delta T_n$, consistent with a reduction in the tendency for heterogeneous nucleation. The $\Delta T_n$ values were found to be 7–39 K without OTS and increased to 67–109 K with OTS for $ZrSiO_4/SiO_2$ face coat-coated crucibles, and from 8–13 K to 26–67 K for pure $Y_2O_3$-coated crucibles. Furthermore, decreasing contact time between CMSX-4 and pure $Y_2O_3$ coating increased the nucleation undercooling from 16–50 K at 2280 seconds to 28–80 K at 1140 seconds, reflecting a greater nucleation barrier due to limited reaction time (Figure 4(b)). Detailed analysis of reaction kinetics affecting these results is discussed further in Section III–C–1.

### B. *Effect of Oxygen Partial Pressure on Metal/Mould Interaction*

The results shown in Figure 4(a) highlight the importance of oxygen partial pressure, which has been further investigated *via* the microstructural analysis presented in this section. When CMSX-4 samples were tested on $ZrSiO_4/SiO_2$ face coat crucibles, aluminium oxide ($Al_2O_3$) was identified in two distinct

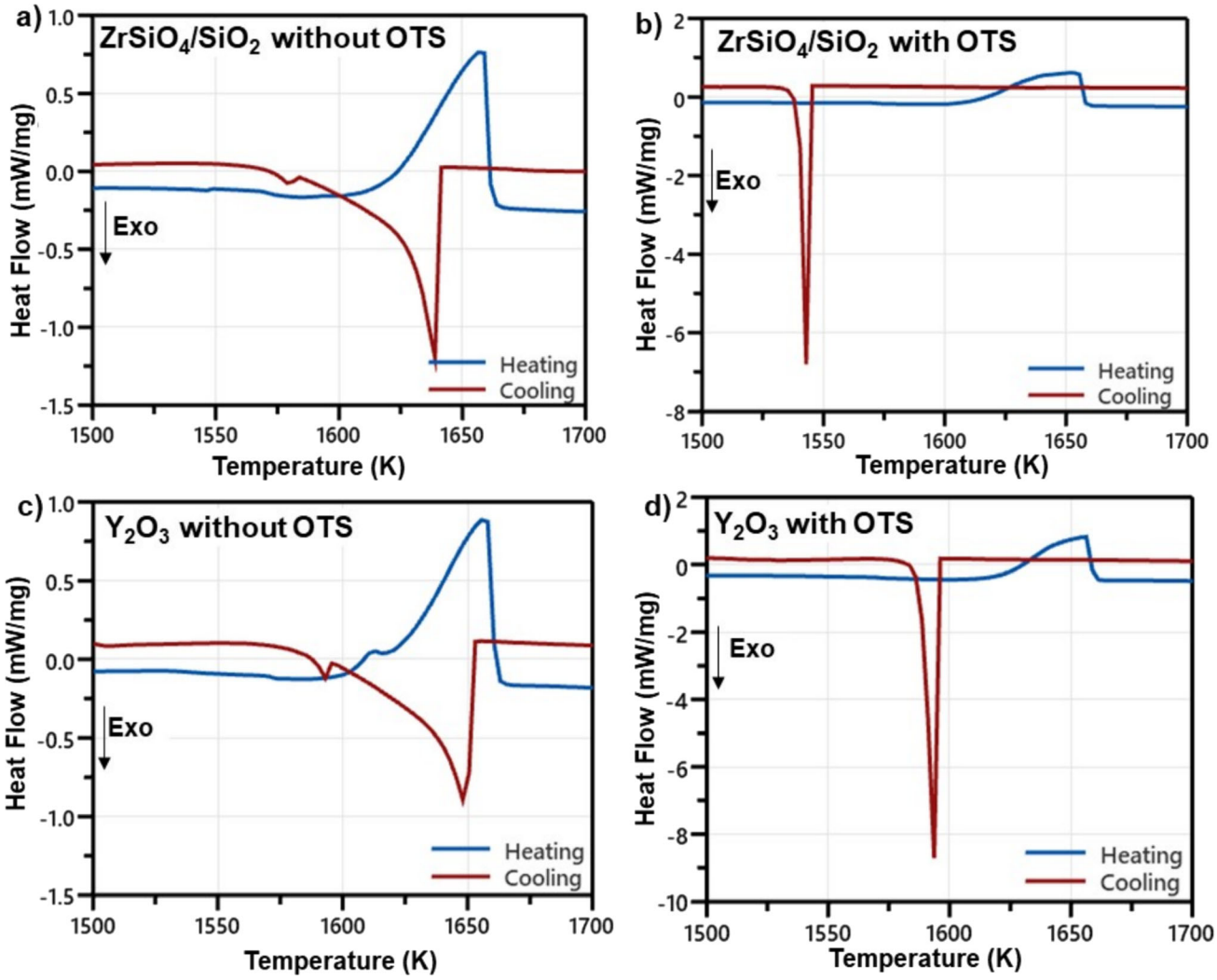


Fig. 3—DSC curves obtained using standard thermal cycle for test conducted without and with oxygen trap system (OTS), (*a*, *b*) crucibles coated with $ZrSiO_4/SiO_2$ face coat, and (*c*, *d*) crucibles coated with pure $Y_2O_3$.

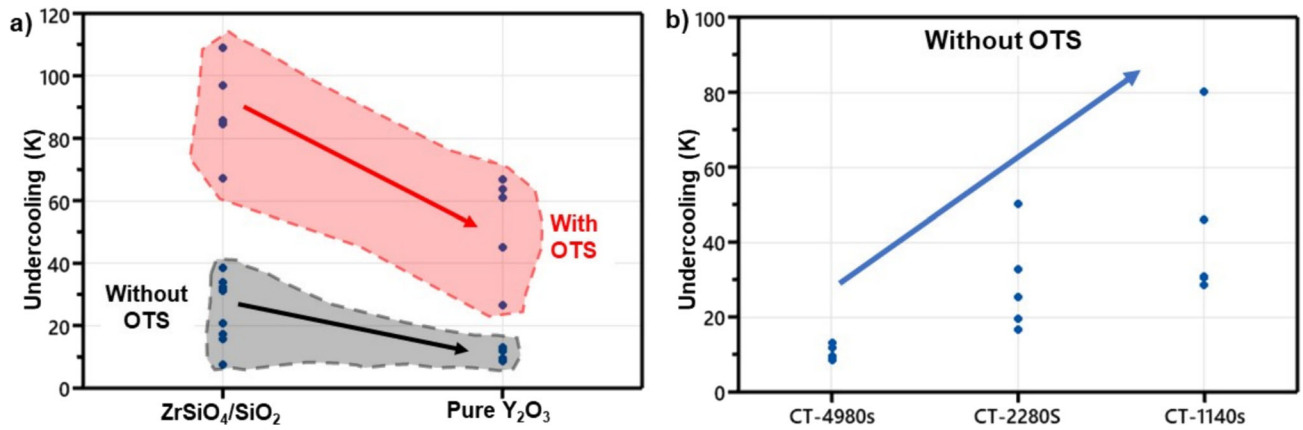


Fig. 4—Nucleation undercooling for CMSX-4 when solidified on (*a*) $ZrSiO_4/SiO_2$ face coat slurry, and pure $Y_2O_3$ without and with oxygen trap system (OTS), and (*b*) pure $Y_2O_3$ as a function of liquid contact time (CT).

morphologies: (i) a continuous, relatively thick layer enveloping the sample surface, including the CMSX-4 and $ZrSiO_4/SiO_2$ coating interface, and (ii) as discrete whisker-like structures. The continuous layer can be attributed to the reaction of molten CMSX-4 with either atmospheric oxygen or the mixed oxides present in the

**Table I. Liquidus Temperature ($T_m$), Solidification Temperature ($T_s$), and Nucleation Undercooling ($\Delta T_n$) Obtained from DSC Signals for With and Without OTS Conditions**

| Test Condition | Liquidus Temperature ($T_m$) | Solidification Temperature ($T_s$) | Nucleation Undercooling ($\Delta T_n$) |
|---|---|---|---|
| $ZrSiO_4/SiO_2$ | 1654 | 1545 | 109 |
| (With OTS) | 1653 | 1567 | 86 |
| | 1656 | 1559 | 97 |
| | 1656 | 1589 | 67 |
| | 1655 | 1571 | 84 |
| $ZrSiO_4/SiO_2$ | 1653 | 1646 | 7 |
| (Without OTS) | 1656 | 1636 | 20 |
| | 1655 | 1640 | 15 |
| | 1655 | 1623 | 32 |
| | 1654 | 1615 | 39 |
| Pure $Y_2O_3$ | 1655 | 1629 | 26 |
| (With OTS) | 1655 | 1610 | 45 |
| | 1656 | 1589 | 67 |
| | 1656 | 1593 | 63 |
| | 1656 | 1595 | 61 |
| Pure $Y_2O_3$ | 1657 | 1644 | 13 |
| (Without OTS) | 1656 | 1648 | 8 |
| | 1657 | 1648 | 9 |
| | 1656 | 1647 | 9 |
| | 1657 | 1645 | 12 |

All values are in kelvin.

**Table II. Liquidus Temperature ($T_m$), Solidification Temperature ($T_s$), and Nucleation Undercooling ($\Delta T_n$) Obtained from DSC Signals for as a Function of Contact Time**

| Test Condition | Liquidus Temperature ($T_m$) | Solidification Temperature ($T_s$) | Nucleation Undercooling ($\Delta T_n$) |
|---|---|---|---|
| Pure $Y_2O_3$ | 1660 | 1644 | 16 |
| (2280 s) | 1659 | 1634 | 25 |
| | 1659 | 1626 | 33 |
| | 1658 | 1639 | 19 |
| | 1660 | 1610 | 50 |
| Pure $Y_2O_3$ | 1657 | 1629 | 28 |
| (1140 s) | 1659 | 1628 | 31 |
| | 1658 | 1627 | 31 |
| | 1659 | 1613 | 46 |
| | 1658 | 1578 | 80 |

All values are in kelvin.

coating. At the CMSX-4 and $ZrSiO_4/SiO_2$ face coat interface, the $Al_2O_3$ layer thickness was measured to be ~ 2.2 $\mu$m in samples processed without the oxygen trap system (OTS) and ~ 1.5 $\mu$m in those with OTS (Figures 5(b) and (d)). Additionally, in the absence of OTS, $Al_2O_3$ whiskers were also observed on the solidified CMSX-4 surface as a result of higher oxygen partial pressure (Figure 5(a)). The formation of metal oxide whiskers is feasible during high-temperature heating as has been reported previously.[28–30] Furthermore, hafnium oxide ($HfO_2$) was consistently observed as a reaction product in all $ZrSiO_4/SiO_2$ face coat-coated crucibles, irrespective of OTS application—in line with the previous observation.[7]

Similar $Al_2O_3$ layers were observed enveloping the CMSX-4 surface, on the top and at the periphery of the CMSX-4 and pure $Y_2O_3$ interface (bottom surface), when solidified without the OTS. Microstructural examination of the periphery region revealed the co-existence of $Al_2O_3$, YAG ($Y_3Al_5O_{12}$), and YAP ($YAlO_3$), as shown in Figure 6(b). In the centre region of the CMSX-4 and pure $Y_2O_3$ interface, a significantly thicker reaction layer (~ 15 $\mu$m) was consistently observed, involving YAP, YAM ($Y_4Al_2O_9$), and residual $Y_2O_3$ (Figure 6(c)). $HfO_2$ was also detected within this reaction layer.

The formation of a substantial reaction layer composed of mixed oxides at the CMSX-4 and pure $Y_2O_3$ interface in samples processed without OTS underlines the critical role of oxygen availability during solidification in governing interfacial reactivity.

In contrast, no $Al_2O_3$ was detected at the CMSX-4 and pure $Y_2O_3$ interface when the oxygen trap system (OTS) was employed. The top surface of the sample appeared clean (free from oxidation), while minor reaction traces were localized near the centre of the CMSX-4 and pure $Y_2O_3$ contact interface, as shown in the inset of Figure 6(d). At the interface, discrete YAG ($Y_3Al_5O_{12}$) particles smaller than 1 $\mu$m were observed. This indicates that the use of zirconium oxygen trap

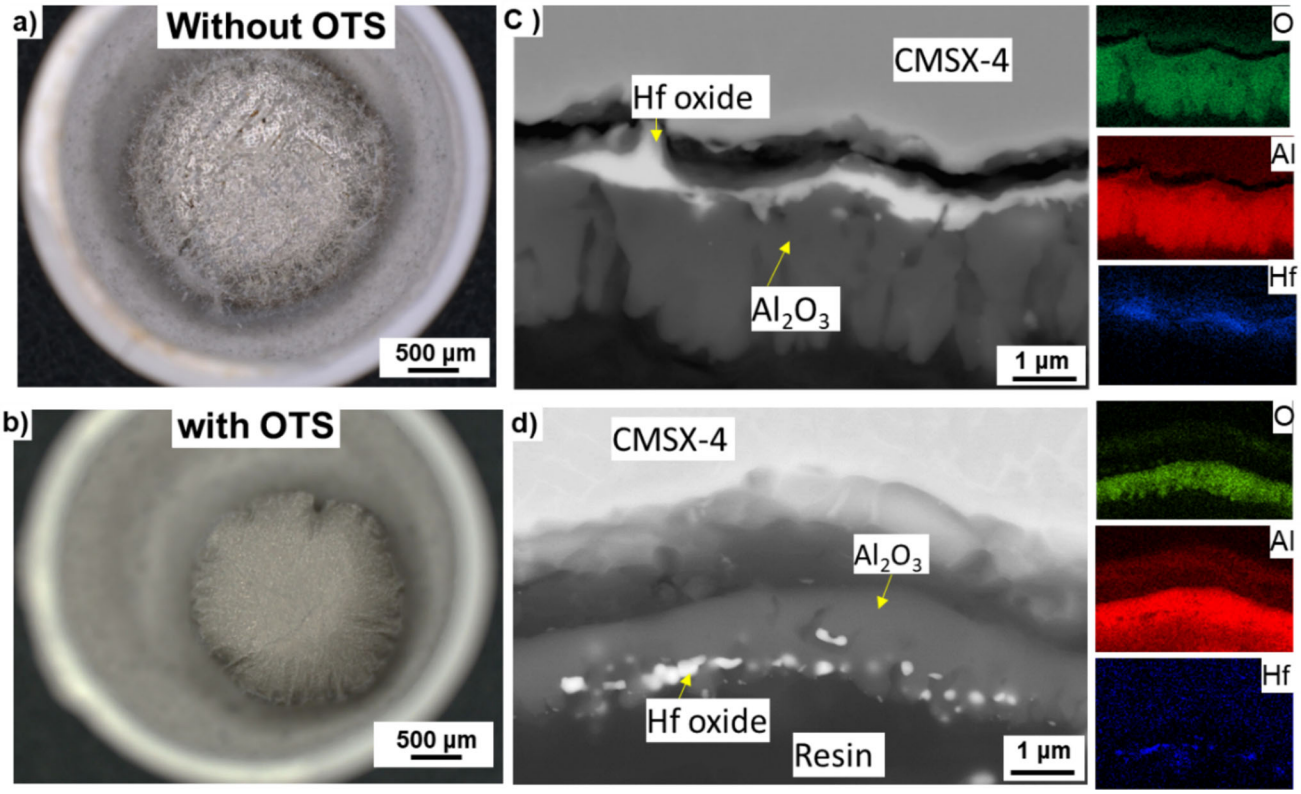


Fig. 5—CMSX-4 after solidification on $ZrSiO_4/SiO_2$ face coat, (*a*, *b*) optical images of the solidified samples without and with OTS, respectively, and (*c*, *d*) BSE micrographs with EDS maps of the perpendicular section of the reaction interface without OTS and with OTS, respectively.

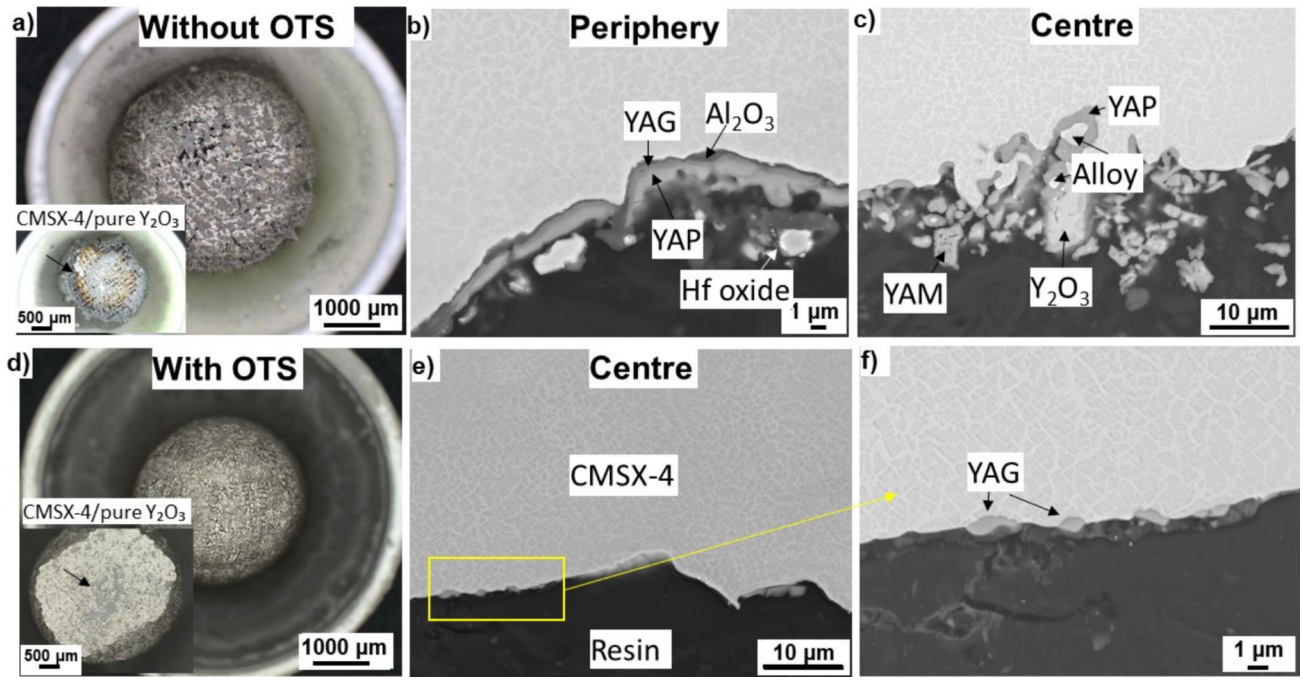


Fig. 6—CMSX-4 after solidification on pure $Y_2O_3$, (*a*, *d*) are the optical images of solidified samples without and with OTS, respectively, and (*b*, *c*, *e*, *f*) BSE micrographs of perpendicular sections of the reaction interface showing the formation of YAG ($Y_3Al_5O_{12}$), YAP ($YAlO_3$), and YAM ($Y_4Al_2O_9$) in the reaction layer of without OTS and YAG ($Y_3Al_5O_{12}$) particles in the reaction layer of with OTS, respectively (Optical images of plan view from bottom are shown in the inset of (a) and (d)).

system effectively reduces the oxygen partial pressure during processing and stabilizes $Y_2O_3$, thereby limiting the reaction of molten CMSX-4 with $Y_2O_3$.

### C. *Detailed Analysis of CMSX-4/pure $Y_2O_3$ Interaction*

Despite the thermodynamic stability of $Y_2O_3$, it was found to be reactive with CMSX-4, and a large reaction layer was observed at CMSX-4 and pure $Y_2O_3$ interface. This section explores the potential interactions between CMSX-4 and pure $Y_2O_3$ in the absence of the oxygen trap system (OTS), which leads to the formation of reaction products such as $HfO_2$, YAP ($YAlO_3$), YAG ($Y_3Al_5O_{12}$), and YAM ($Y_4Al_2O_9$).

The CMSX-4 superalloy contains multiple reactive alloying elements, including Al and Hf, both of which exhibit a strong tendency to form stable oxides such as $Al_2O_3$ and $HfO_2$. Among these, $HfO_2$ is highly stable and was found in the interface reaction layer during tests conducted without the oxygen trap system (OTS), although Hf is present in the alloy at only 0.1 wt pct. The formation of $HfO_2$ on superalloy surfaces during casting has been reported previously.[7]

Aluminium in CMSX-4 also reacts readily with available oxygen in the furnace atmosphere under no OTS conditions, resulting in the formation of $Al_2O_3$. The presence of $Al_2O_3$ exclusively at the periphery of CMSX-4 and pure $Y_2O_3$ interface—but not at the centre—suggests that $Al_2O_3$ formation is primarily due to the reaction with atmospheric oxygen rather than direct reaction with $Y_2O_3$ (Figures 6(a) through (c)). This is supported by the fact that while $Y_2O_3$ is present across the entire bottom surface, oxygen ingress from the furnace is limited to the outer edge.

Thus, at the periphery, a sequence of reactions occurs: Al in CMSX-4 first reacts with atmospheric oxygen to form $Al_2O_3$ (Reaction [1]), which subsequently reacts with $Y_2O_3$ to form YAP ($YAlO_3$) *via* Reaction [2]. YAP then further reacts with $Al_2O_3$ to form YAG ($Y_3Al_5O_{12}$) as shown in Reaction [3]. This sequential transformation leads to the co-existence of $Al_2O_3$, YAP, and YAG in the outer reaction layer (Figure 6(b)):

$$2Al(l) + 3O_2(g) \rightarrow Al_2O_3(s) \quad [1]$$

$$Al_2O_3(s) + Y_2O_3(s) \rightarrow 2YAlO_3(s) \quad [2]$$

$$Al_2O_3(s) + 3YAlO_3(s) \rightarrow Y_3Al_5O_{12}(s). \quad [3]$$

At the centre of the CMSX-4 and $Y_2O_3$ interface—where furnace oxygen is minimal—$Y_2O_3$ reacts directly with Al in molten CMSX-4, resulting in the formation of YAM ($Y_4Al_2O_9$) and YAP, as given in reactions 4 and 6. Once formed, YAM can further react with Al to yield YAP, as described in Reaction [5]. The observation of YAM surrounding YAP in several regions suggests a transformation pathway from YAM to YAP. Additionally, the presence of YAP particles adjacent to the metal indicates direct formation *via* reaction between $Y_2O_3$ and Al (Reaction [6]). The formation of YAP, YAG, and YAM from the high-temperature interaction between $Y_2O_3$ and $Al_2O_3$, and $Y_2O_3$ and pure Al has been reported previously.[31–35] The overall reactions involved are as follows:

$$3Y_2O_3(s) + 2Al(l) \rightarrow Y_4Al_2O_9(s) + 2Y \quad [4]$$

$$Y_4Al_2O_9(s) + Al(l) \rightarrow 3YAlO_3(s) + Y \quad [5]$$

$$Y_2O_3(s) + Al(l) \rightarrow YAlO_3(s) + Y \quad [6]$$

$$4YAlO_3(s) + Al(l) \rightarrow Y_3Al_5O_{12}(s) + Y \quad [7]$$

In order to validate the transformation sequence discussed above, the interfacial reactions at the CMSX-4 and pure $Y_2O_3$ interface were investigated for the DSC tests performed with a reduced liquid contact time.

At a contact time of 2280 seconds (almost half of the standard thermal cycle), co-existence of YAG and YAP was observed at the CMSX-4 and pure $Y_2O_3$ interface, with no detectable $Al_2O_3$; YAG is found at the metal side and YAP at the coating interface (see Figure 7(a)). Even at this intermediate contact time, untransformed YAP and regions containing YAP + YAM + $Y_2O_3$ were still observed—similar to the longer contact time condition—highlighting the incomplete transformation to YAG. This suggests that YAG can also form from the reaction between YAP and Al in molten CMSX-4 (as per Reaction [7]), indicating a transformation occurring later in the sequence. When the contact time was further reduced to 1140 seconds, the reaction layer consisted mainly of well-separated YAP particles in the central region (Figure 7(b)), with co-existing YAP + YAM + $Y_2O_3$ phases observed near the periphery. YAG was largely absent in these samples, again highlighting the conclusion that YAG forms at a later stage. The reaction products at the CMSX-4 and pure $Y_2O_3$ interface are summarized as a function of contact time and undercooling in Figure 8.

### D. *$Y_2O_3/ZrSiO_4/SiO_2$ Face Coat*

Whilst the effect of pure $Y_2O_3$ as a face coat has been established, its efficacy when incorporated into the standard $ZrSiO_4/SiO_2$ face coat slurry remains unclear particularly in terms of interfacial reactivity and its influence on $\gamma$-grain nucleation. To investigate this, a modified face coat was prepared by doping the standard slurry with 4.5 wt pct $Y_2O_3$.

Interestingly, a marked increase in $\Delta T_n$ to 22.6–86 K is observed when CMSX-4 was solidified on $Y_2O_3$-doped $ZrSiO_4/SiO_2$ face coat. This value is significantly higher than that for pure $Y_2O_3$ face coat (8–13 K) and undoped $ZrSiO_4/SiO_2$ face coat (7–39 K). Therefore, the incorporation of $Y_2O_3$ into the $ZrSiO_4/SiO_2$ face coat slurry would appear to make the standard slurry less potent with respect to the heterogeneous nucleation of Ni $\gamma$-grains.

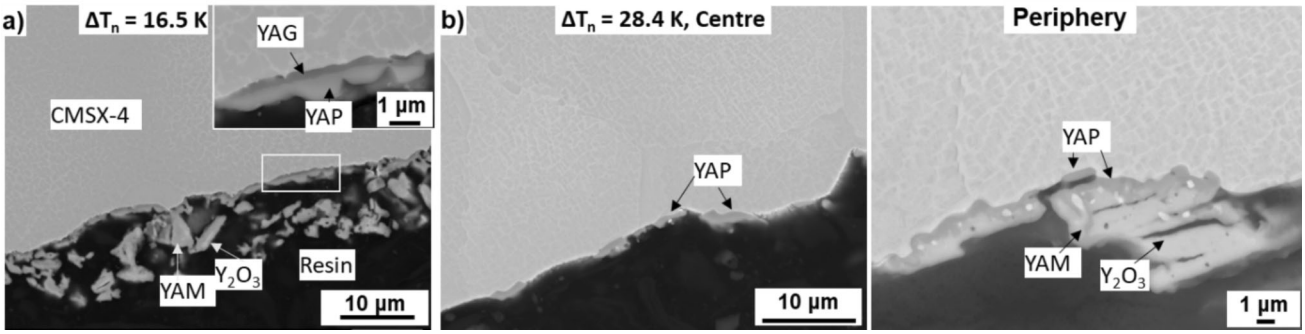


Fig. 7—BSE micrographs of the CMSX-4 and pure $Y_2O_3$ contact interface at different liquid contact times corresponding to the lowest undercooling in each case, (*a*) at contact time 2280 s, and (*b*) at contact time 1140 s, left image in (b) is from centre region and right image is from periphery.

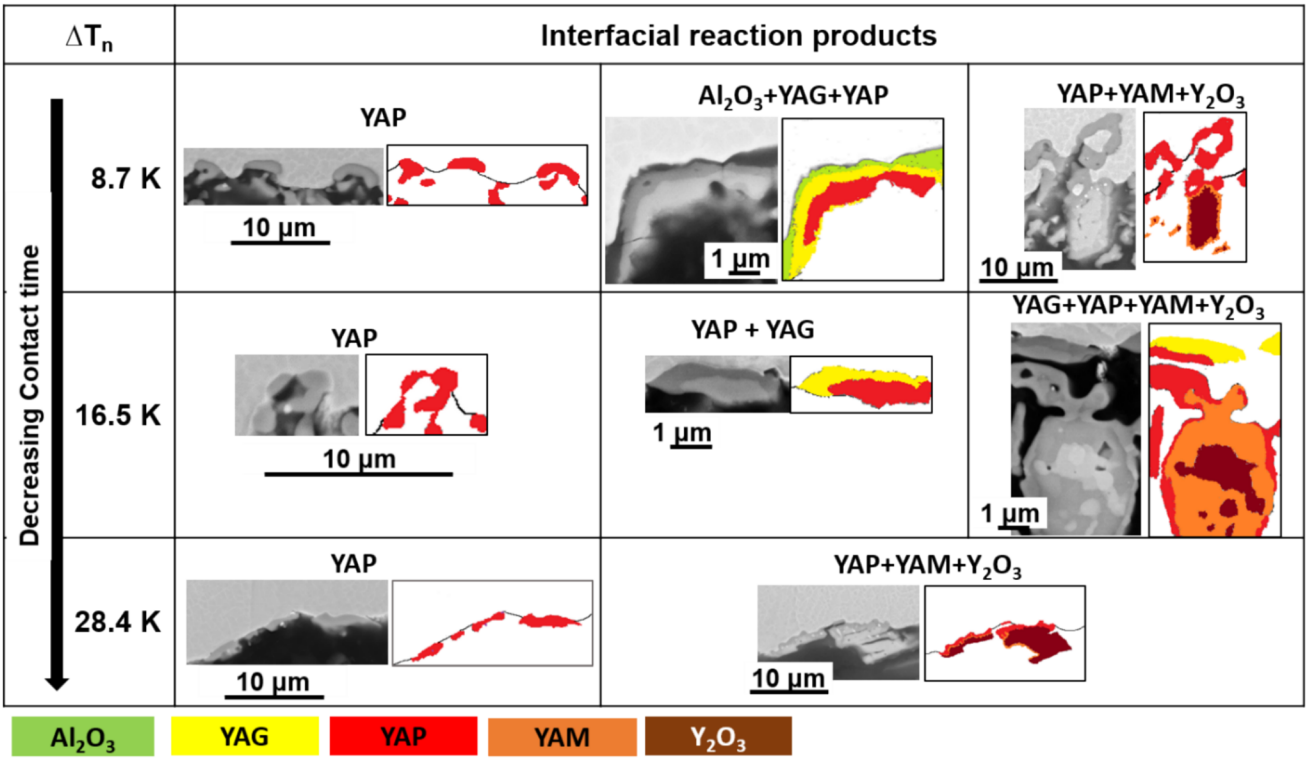


Fig. 8—BSE micrographs with their coloured representative images showing different appearances of the reaction products at different locations of the CMSX-4/coating interface as a function of contact time and undercooling (Note: $HfO_2$ is found in the reaction layer in every case and is not included in this image.).

Microstructural characterization of the solidified CMSX-4 sample revealed the formation of a continuous $Al_2O_3$ layer, approximately 10 $\mu$m thick, enveloping the sample surface (Figure 9(a)). At the periphery of the CMSX-4 and face coat contact interface, a network of YAG embedded within the $Al_2O_3$ layer was observed, along with dispersed $ZrO_2$ particles coexisting with both YAG and $Al_2O_3$. In contrast, no reaction products were observed at the centre region of the bottom surface of the CMSX-4, as shown in Figure 9(b) and (c). The observed interfacial reactions indicating the significance of $Al_2O_3$ in destabilizing the $Y_2O_3$-doped $ZrSiO_4/SiO_2$ face coat.

## IV. DISCUSSION

The results presented above offer valuable insights but also raise several important issues. For example (1) how do the solidification conditions—particularly oxygen partial pressure, and heating/cooling rate—in the Bridgman casting furnace compared to those used in the DSC experiments? (2) Do the observed reaction products correspond to final equilibrium phases, or could they instead be metastable as transient phases formed under specific processing conditions? (3) What is the thermodynamic and kinetic stability of mould formulation for casting CMSX-4 alloy? In order to address these questions, further work has been carried out to compare

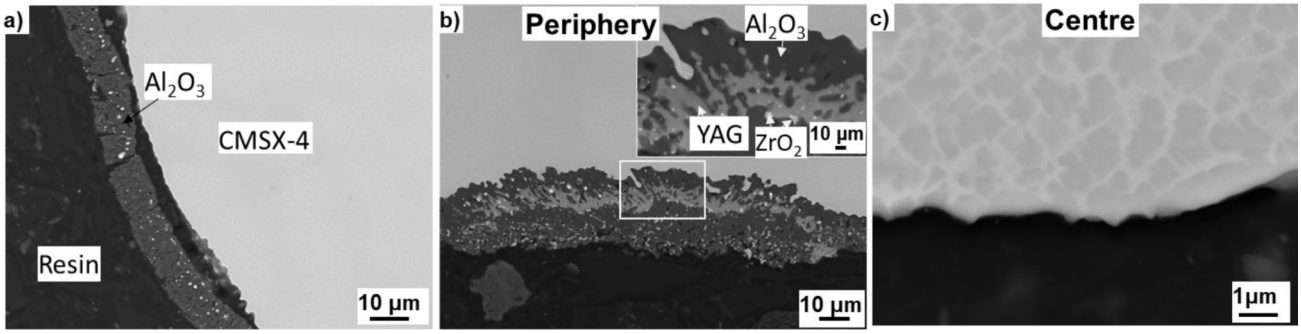


Fig. 9—BSE micrograph of the CMSX-4 after solidification on $Y_2O_3$-doped $ZrSiO_4/SiO_2$ face coat, (*a*) $Al_2O_3$ layer formed sample free surface, and (*b*, *c*) perpendicular section of the reaction interface at the periphery and the centre region, respectively.

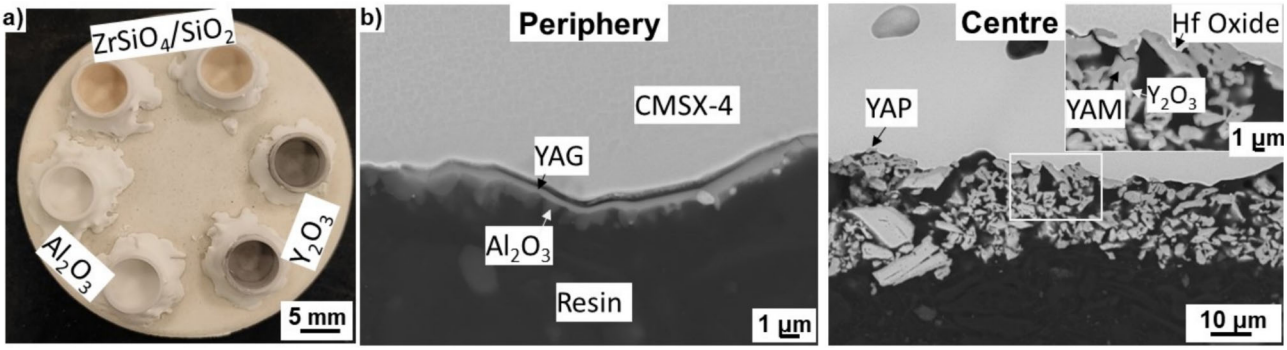


Fig. 10—(*a*) Face coat-coated DSC crucibles mounted on ceramic plate for solidification in Bridgman casting furnace, (*b*) BSE micrograph of the perpendicular section of the reaction interface between CMSX-4 and pure $Y_2O_3$ face coat.

the thermal/chemical environments of the DSC and casting furnace, and to evaluate the thermodynamic feasibility of the interfacial reaction products.

### A. *Validation with Bridgman Casting Furnace*

DSC crucibles uncoated (alumina), coated with $ZrSiO_4/SiO_2$ face coat, and pure $Y_2O_3$ face coat—each containing CMSX-4 samples—were solidified in a Bridgman casting furnace as shown in Figure 10(a). After solidification, the CMSX-4 samples were examined to compare the reaction products resulting from CMSX-4 and face coat interaction under DSC (as previously) and furnace conditions. In line with the focus of this study, particular attention is given to the furnace-solidified CMSX-4 on pure $Y_2O_3$ face coat. Co-existence of $Al_2O_3$ and YAG is observed at the periphery of the solidified CMSX-4; however, at the centre of the CMSX-4 and pure $Y_2O_3$ coating interface, a large reaction layer of ~ 20 $\mu$m thickness and composed of YAP, YAM, and untransformed $Y_2O_3$ is confirmed (as shown in Figure 10(b)).

The obtained reaction layer—regarding thickness, composition, and morphology—closely resembles that observed under DSC conditions without the oxygen trap system (compare Figures 6(c) and 10(b)). This indicates that the furnace environment of the DSC without the oxygen trap system and with the standard thermal cycle closely resembles the Bridgman casting experiments.

A key observation is that the chemical stability of both the $ZrSiO_4/SiO_2$ face coat and the pure $Y_2O_3$ face coat increases with decreasing oxygen partial pressure in the furnace. This effect is evident in two ways: (1) higher nucleation undercooling ($\Delta T_n$) values are observed when OTS is used, and (2) reduced interfacial reactivity between CMSX-4 and the face coat, consistent with increased inertness of these oxide coatings under low oxygen partial pressures. The influence of environmental oxygen on undercooling has been reported previously using DSC on high-purity gold and a significant drop in undercooling was reported when 500 ppm oxygen was incorporated with Ar during solidification.[4] Similarly, a decrease in undercooling with increasing $pO_2$ was reported for Fe and Ni solidified on various substrates, attributed to reduced wetting contact angles.[9,36,37] The present results highlight the critical role of impurities in mould materials in influencing heterogeneous nucleation. It is also worth mentioning that the DSC experiments closely mimic the single-crystal casting method when the OTS is omitted. For instance, the DSC crucibles were prepared identically to the investment casting mould, involving pre-firing in air, and using CMSX-4 samples from the same CMSX-4® master ingot with less than 1 ppm oxygen concentration. Using differential scanning calorimetry (DSC) offers a practical alternative to complex sessile drop experiments; however, the use of DSC inherently limits the ability to perform contact angle measurements.

To summarize, the results presented provide direct evidence that reducing oxygen partial pressure during the solidification of CMSX-4 on mixed-oxide face coats significantly increases $\Delta T_n$ and may thereby improve the quality and uniformity of the castings.

### B. *Alloy–Ceramic Interaction Model*

The formation of reaction products from metal–mould interactions highlights the importance of evaluating the thermodynamic and kinetic stability of the face coats. In particular, the role of oxygen and aluminium in CMSX-4 appears pivotal in driving the equilibrium towards dissolution of $Y_2O_3$ when pure $Y_2O_3$ face coat is used as a mould. However, a central question is whether the reaction products—YAG ($Y_3Al_5O_{12}$), YAM ($Y_4Al_2O_9$), and YAP ($YAlO_3$)—are stable equilibrium phases or else metastable intermediates formed during transient stages of the reaction. The function of $Y_2O_3$ as an additive to the $ZrSiO_4/SiO_2$ system also warrants closer examination, particularly regarding the broader range of reaction products it induces. A detailed analysis of dissolution kinetics and subsequent phase formation addresses these questions, especially in establishing the stability hierarchy of the resulting phases and identifying the dominant and subordinate products involved in the reaction's progression.

To investigate these findings further, the Kampmann–Wagner model[38] was modified to simulate the multi-component interaction between CMSX-4 liquid melt and oxide particles. In the simulation, one or more spherical oxide particles were embedded within a spherical liquid domain representing the CMSX-4 superalloy composition. The rate of change in particle radius $r$ is assumed to be governed by diffusion of elements in the liquid phase and the free energy change of reaction ($\Delta G_r$) as shown in Eq. [1].

$$\frac{dr}{dt} = \frac{D}{r} \cdot \frac{\Delta G_r}{RT}, \quad [1]$$

where $D$ is the diffusion of solute in the liquid, $r$ is the radius, and $\Delta G_r$ is normalized by gas constant $R$ and temperature $T$. The sign of $\Delta G_r$ was used to determine the direction of the reaction—negative $\Delta G_r$ causes particle shrinkage, indicating instability—positive $\Delta G_r$ results in particle growth, signifying a stable, growing oxide—$\Delta G_r$ of zero indicates equilibrium between the particle and the liquid. The driving force $\Delta G_r$ was calculated based on the chemical activities of elements in the liquid at each time consistent with

$$\frac{\Delta G_r}{RT} = \ln\left(\frac{a_O \cdot a_M}{a_O^e \cdot a_M^e}\right), \quad [2]$$

where $a_O$ and $a_M$ are the chemical activities of oxygen (O) and metal (M) in the liquid phase and $a_O^e$ and $a_M^e$ are the equilibrium activities of oxygen and metal. The activities were calculated through TCNI8 database* using mol fractions of elements in the liquid calculated after each time-step as shown in Eq. [3]:

$$x_{i,l} = \frac{x_{i,0} - (f_{sol} \cdot x_{i,s}) - (f_{sol2} \cdot x_{i,s2}) - (f_{sol3} \cdot x_{i,s3})}{f_{liq}}, \quad [3]$$

where $x_{i,l}$ is the fraction of element $i$ in liquid, $x_{i,0}$ is the nominal alloy composition of the element i, $f_{sol}$, $f_{sol2}$, and $f_{sol3}$, are the phase fractions of the three solid particles and $f_{liq}$ is the fraction of liquid $x_{i,s}$, $x_{i,s2}$, and $x_{i,s3}$, are the corresponding stoichiometric composition of element $i$ in their respective particles.

The composition changes due to particle growth or dissolution directly influences $\Delta G_r$ at each time-step, creating a feedback loop between particle evolution and the surrounding melt. The updated solute composition in Eq. [3] is then used to query the TCOX11 database for phases that are thermodynamically stable through an equilibrium calculation. Assuming no kinetic barrier to nucleation, these new phases are introduced into the liquid, enabling further growth and phase evolution. In the present study, the interaction between liquid CMSX-4 with $Y_2O_3$ particle, and $Y_2O_3/ZrSiO_4/SiO_2$ oxide particles (in the ratio similar to the experimental $Y_2O_3$-doped $ZrSiO_4/SiO_2$ face coat) at 1763K are emphasized.

The stability and reactivity of $Y_2O_3$ in contact with CMSX-4 were found to be highly sensitive to the oxygen concentration in the melt. At a low oxygen content ($1 \times 10^{-4}$ mol fraction), $Y_2O_3$ remains stable (see Figure 11(a)), consistent with its known thermodynamic stability. However, increasing the oxygen level to $1 \times 10^{-3}$ mol fraction results in its initial destabilization as shown in Figure 11(b), highlighting the critical role of oxygen in driving oxide–metal interactions. This behaviour underscores the importance of tightly controlling oxygen levels during casting to prevent unwanted degradation of otherwise stable mould materials.

Upon destabilization, yttrium and oxygen released into the melt promote the formation of complex aluminium-based oxides: YAG ($Y_3Al_5O_{12}$), YAM ($Y_4Al_2O_9$), and YAP ($YAlO_3$), as shown in Figure 11(c). These phases incorporate aluminium from the CMSX-4 itself, reflecting a dynamic exchange between the mould and the melt. Among these, YAG was identified as the dominant product, forming more readily than YAM and YAP. This hierarchy in growth rates is likely influenced by differences in thermodynamic stability and the local chemical environment, and it plays a crucial role in dictating the sequence of phase formation.

The tendency of these secondary oxides to form appears to be a key driving force for the dissolution of $Y_2O_3$, shifting the system away from its initial equilibrium. These predictions are consistent with experimental observations: higher undercooling values were recorded for $Y_2O_3$ when an oxygen-trapping system was employed, indicating greater stability under reduced oxygen conditions, while lower undercooling in the absence of such a system corresponded to increased reactivity and product formation.

*TCNI8 and TCOX11 databases are software products developed by Thermo-Calc Software AB

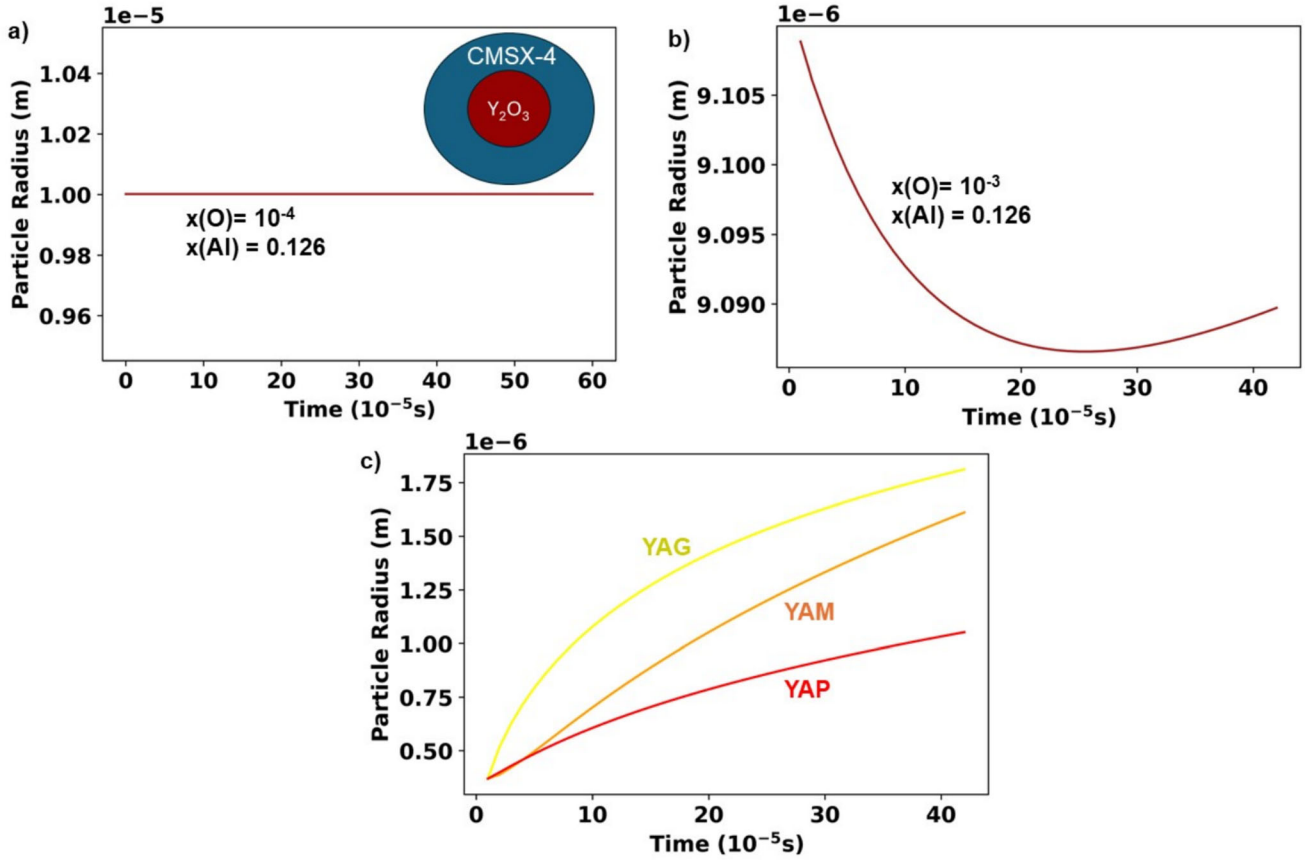


Fig. 11—Interaction between pure $Y_2O_3$ and liquid CMSX-4 at 1763 K, (*a*) showing no change in system dynamics with an oxygen mol fraction of $10^{-4}$, (*b*) showing $Y_2O_3$ destabilization with an oxygen mol fraction of $10^{-3}$, and (*c*) formation of reaction products YAG, YAM, and YAP following $Y_2O_3$ dissolution.

The simulation results of the $ZrSiO_4/SiO_2$ face coat system with 4.5 pct $Y_2O_3$ reveal a significant chemical interaction with liquid CMSX-4. All three primary oxides—$ZrSiO_4$, $SiO_2$, and $Y_2O_3$—are found to dissolve progressively upon contact with the melt. This dissolution results in the release of Zr, Si, O, and Y into the liquid alloy, fundamentally altering the chemical composition in the liquid, which initially facilitates the growth of YAG and $Al_2O_3$. YAG forms early in the reaction due to the availability of both yttrium from the dissolving $Y_2O_3$ and Al from CMSX-4. However, YAG is later observed to dissolve back into the melt, suggesting that it is not thermodynamically stable under sustained reaction conditions. In contrast, $Al_2O_3$ continues to grow, ultimately becoming the dominant phase, indicating higher thermodynamic stability in this environment. As the reaction progresses, $ZrO_2$ begins to nucleate. It first appears in the tetragonal phase before transitioning to growth in the fluorite structure, as shown in Figure 12. The reaction products identified are same as those observed in experiments as shown in Figure 9.

The results demonstrate a complex dynamic response of the system to changes in local chemistry driven by dissolution and reprecipitation. They also offer mechanistic insight, revealing that the formation of these secondary phases is not a consequence of direct solid-state reactions but is instead driven by the chemical instability and dissolution of the primary mould oxides into the CMSX-4 melt. The modelling findings not only reproduce the experimentally observed reaction products but also raises the question of how mould instability gives rise to microstructural consequences.

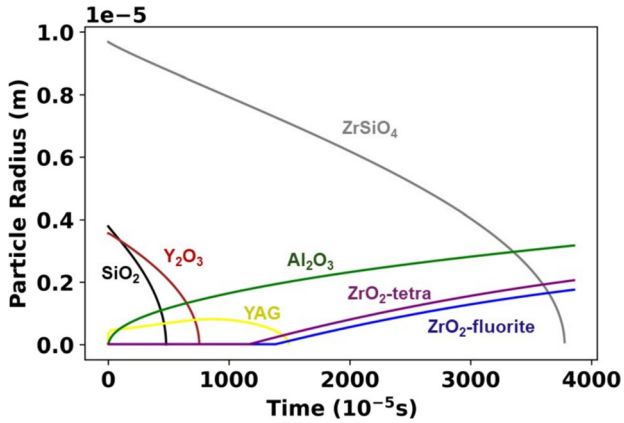


Fig. 12—Interaction between face coat ($ZrSiO_4/SiO_2$/4.5 wt pct $Y_2O_3$) and liquid CMSX-4, showing face coat dissolution followed by growth of YAG, $Al_2O_3$, and $ZrO_2$, at 1763 K.

Importantly, these reaction products are not merely passive consequences of oxide instability; they may actively influence the nucleation behaviour of the $\gamma$-phase in CMSX-4, as observed in DSC experiments. The presence of secondary oxides introduces local chemical and structural discontinuities, which can lower the nucleation energy barrier by providing energetically favourable surfaces for the initial formation of solid $\gamma$-phase nuclei. However, controlled and predictable reactivity of the mould face coat may not necessarily be detrimental. On the contrary, intentionally leveraging certain reaction products as nucleation promoters could be a strategic approach to refining grain structure and improving casting quality.

## V. SUMMARY AND CONCLUSIONS

The research presented here can be summarized as follows:

1. An experimental approach is proposed to assess the potency of heterogeneous nucleation occurs *via* the presence of phases in the ceramic mould and specifically a face coat. Precision is assured by making use of instrumentation in a differential scanning calorimeter (DSC).
2. The range of undercoolings we have detected is substantial but in the case of pure $Y_2O_3$ face coat in contact with CMSX-4 is very low at $< 10$ K. Consistent with $Y_2O_3$ being highly reactive with CMSX-4, we have observed complex oxides of Y and Al including YAP ($YAlO_3$), YAG ($Y_3Al_5O_{12}$), and YAM ($Y_4Al_2O_9$).
3. We have observed also a potent influence of oxygen by making use of an oxygen trap system; the undercooling needed for gamma grain nucleation in CMSX-4 decreases from 67–109 to 7.4–39 K for standard $ZrSiO_4/SiO_2$ face coat, and from 26–67 to 8–13 K for pure $Y_2O_3$ face coat when oxygen levels are higher.
4. With decreasing liquid metal contact time, the chemistry of the interfacial reaction products and their distribution change; this indicates a reduced probability of a heterogeneous nucleation site consistent with the observed increase in nucleation undercooling.
5. The experiments with decreasing liquid metal contact time can be used to understand the transformation kinetics. We have identified the most probable transformation sequences at CMSX-4/pure $Y_2O_3$ contact interface.
6. The experimental approach proposed has been compared with results derived using industrial-scale Bridgman single-crystal casting furnace with consistency demonstrated.
7. A thermodynamic and kinetic model developed to simulate multi-component interactions between oxides and metals, including the formation of secondary phases, demonstrates good agreement with the experimental observations.


## ACKNOWLEDGMENT

The authors thank Rolls-Royce plc and the Engineering and Physical Sciences Research Council for their financial support under Prosperity Partnership grant reference EP/X025454/1, Advanced Research into Crystallographic Anisotropy & Nucleation Effects in single crystals (ARCANE). Roger Reed also acknowledges the financial support of Rolls-Royce and the Royal Academy of Engineering of his Research Chair in Nickel-Based Superalloys for Next-Generation Aircraft Propulsion.


## DATA AVAILABILITY

The data supporting the findings of this study are available from the corresponding author upon reasonable request.

## CONFLICT OF INTEREST

The authors declare that they have no known competing financial interests or personal relationships that could have appeared to influence the work reported in this paper.



## REFERENCES


1. D. Kashchiev: *Nucleation: Basic Theory with Applications*. Butterworth-Heinemann, Oxford, 2000, pp. 45–57.
2. W. Kurz and D.J. Fisher: *Fundamentals of Solidification*, Trans Tech Publications, Fourth, 1984.
3. D. Kashchiev: *Nucleation: Basic Theory with Applications*, Butterworth-Heinemann, 2000, pp. 9–16.
4. J.H. Perepezko and G. Wilde: *Curr. Opin. Solid State Mater. Sci.*, 2016, vol. 20, pp. 3–12. https://doi.org/10.1016/j.cossms.2015.07.001.
5. B.A. Mueller and J.H. Perepezko: *Metall. Trans. A*, 1987, vol. 18A, pp. 1143–50.
6. D. Giuranno, E. Ricci, E. Arato, and P. Costa: *Acta Mater.*, 2006, vol. 54, pp. 2625–30. https://doi.org/10.1016/j.actamat.2006.02.005.

7. M. Akmal, D.S. Kang, H. Lee, D.W. Yun, H.W. Jeong, Y.S. Yoo, and S.M. Seo: *J. Alloys Compd.*, 2024, https://doi.org/10.1016/j.jallcom.2024.174735.
8. D. Wang, W. Chang, J. Sun, C. Sheng, Y. Zhang, and Q. Zhai: *IOP. Conf. Ser. Mater. Sci. Eng.*, 2018, https://doi.org/10.1088/1757-899X/381/1/012058.
9. M.E. Valdez, P. Uranga, and A.W. Cramb: *Metall. Mater. Trans. B*, 2007, vol. 38B, pp. 257–66. https://doi.org/10.1007/s11663-006-9018-x.
10. Y. Li, Y. Tan, D. Wang, P. Li, Z. Chen, J. Zhao, and J. Qiang: *Corros. Sci.*, 2023, https://doi.org/10.1016/j.corsci.2023.111370.
11. D. Turnbull: *J. Appl. Phys.*, 1950, vol. 21, pp. 1022–28. https://doi.org/10.1063/1.1699435.
12. D. Turnbull: *Acta Metall.*, 1953, vol. 1, pp. 8–14.
13. A.L. Greer, P.S. Cooper, M.W. Meredith, W. Schneider, P. Schumacher, J.A. Spittle, and A. Tronche: *Adv. Eng. Mater.*, 2003, vol. 5, pp. 81–91. https://doi.org/10.1002/adem.200390013.
14. T.E. Quested and A.L. Greer: *Acta Mater.*, 2005, vol. 53, pp. 2683–692. https://doi.org/10.1016/j.actamat.2005.02.028.
15. M. Qian: *Acta Mater.*, 2007, vol. 55, pp. 943–53. https://doi.org/10.1016/j.actamat.2006.09.016.
16. Z. Kožíšek: *J. Cryst. Growth*, 2019, vol. 522, pp. 53–60. https://doi.org/10.1016/j.jcrysgro.2019.06.007.
17. Z. Fan: *Metall. Mater. Trans. A*, 2013, vol. 44A, pp. 1409–18. https://doi.org/10.1007/s11661-012-1495-8.
18. Z. Fan and F. Gao: *Metals (Basel)*, 2022, https://doi.org/10.3390/met12101728.
19. R.C. Reed: *Superalloys—Fundamentals and Applications, First*, Cambridge University Press, Cambridge, 2006.
20. R.E. Napolitano and R.J. Schaefer: *J. Mater. Sci.*, 2000, vol. 35, pp. 1641–59.
21. A. De Bussac and C.-A. Gandin: *Mater. Sci. Eng. A*, 1997, vol. 237, pp. 35–42.
22. N. D'souza, P.A. Jennings, X.L. Yang, H.B. Dong, P.D. Lee, and M. Mclean: *Metall. Mater. Trans. B*, 2005, vol. 36B, pp. 657–66.
23. X. Zhu, F. Wang, and D. Ma: *Materials*, 2023, vol. 16, p. 4112. https://doi.org/10.3390/ma16114112.
24. C.S. Kanetkar, A.S. Kacar, and D.M. Stefanescu: *Metall. Trans. A*, 1988, vol. 19A, pp. 1833–839.
25. G. Brewster, N. D'Souza, K.S. Ryder, S. Simmonds, and H.B. Dong: *Metall. Mater. Trans. A*, 2012, vol. 43, pp. 1288–302. https://doi.org/10.1007/s11661-011-1027-y.
26. Q. Li, H. Zhang, M. Gao, J. Li, and H. Zhang: *J. Mater. Process. Technol.*, 2021, https://doi.org/10.1016/j.jmatprotec.2021.117094.
27. Y. Zi, J. Meng, C. Zhang, Y. Zhou, and Y. Ding: *Acta Metall. Sin. (Engl. Lett.)*, 2020, vol. 33, pp. 1021–30. https://doi.org/10.1007/s40195-020-01030-2.
28. R.C. Devries and G.W. Sears: *J. Chem. Phys.*, 1959, vol. 31, pp. 1256–257. https://doi.org/10.1063/1.1730579.
29. P.L. Edwards and R.J. Happel: *J. Appl. Phys.*, 1962, vol. 33, pp. 826–27. https://doi.org/10.1063/1.1777173.
30. T.H. Ludwig and H. Tohmyoh: *J. Cryst. Growth*, 2022, https://doi.org/10.1016/j.jcrysgro.2022.126849.
31. A.S. Gandhi and C.G. Levi: *J. Mater. Res.*, 2005, vol. 20, pp. 1017–025. https://doi.org/10.1557/JMR.2005.0133.
32. J. Wojewoda-Budka, N. Sobczak, and J. Morgiel: *J. Microsc.*, 2010, vol. 237, pp. 253–57. https://doi.org/10.1111/j.1365-2818.2009.03237.x.
33. J. Wojewoda-Budka, N. Sobczak, B. Onderka, J. Morgiel, and R. Nowak: *J. Mater. Sci.*, 2010, vol. 45, pp. 2042–50. https://doi.org/10.1007/s10853-009-4135-y.
34. D. Zhao, T.W. Coyle, and K. Chien: *Surf. Coat. Technol.*, 2013, vol. 235, pp. 303–09. https://doi.org/10.1016/j.surfcoat.2013.07.058.
35. O. Fabrichnaya, H.J. Seifert, T. Ludwig, F. Aldinger, and A. Navrotsky: *Scand. J. Metall.*, 2001, vol. 30, pp. 175–83. https://doi.org/10.1034/j.1600-0692.2001.300308.x.
36. S. Ueda, H. Shi, X. Jiang, H. Shibata, and A.W. Cramb: *Metall. Mater. Trans. B*, 2003, vol. 34, pp. 503–08.
37. M.E. Valdez, P. Uranga, K. Fuchigami, H. Shibata, and A.W. Cramb: *Metall. Mater. Trans. B*, 2006, vol. 37B, pp. 811–21.
38. L. Ratke and P.W. Voorhees: *Growth and Coarsening*, Springer, Berlin, 2002, pp. 57–95.